

# JGR Space Physics

## RESEARCH ARTICLE

10.1029/2021JA029737

### Key Points:

- Plasmatrough electron density equations in the SPM model are revisited with new parametrization using data from Van Allen Probes mission
- The new parametrized equations provide improved data for high  $L$  values ( $L > 3$ ) and high geomagnetic activity
- Refilling mechanisms through a thicker plasmasphere boundary layer must be taken into account for quiet periods after erosion

### Correspondence to:




E. Botek,  
[edith.botek@aeronomie.be](mailto:edith.botek@aeronomie.be)

### Citation:

Botek, E., Pierrard, V., & Darrouzet, F. (2021). Assessment of the Earth's cold plasmatrough modeling by using Van Allen Probes/EMFISIS and Arase/PWE electron density data. *Journal of Geophysical Research: Space Physics*, 126, e2021JA029737. <https://doi.org/10.1029/2021JA029737>

Received 1 JUL 2021  
Accepted 11 NOV 2021

## Assessment of the Earth's Cold Plasmatrough Modeling by Using Van Allen Probes/EMFISIS and Arase/PWE Electron Density Data

E. Botek<sup>1</sup> , V. Pierrard<sup>1,2</sup> , and F. Darrouzet<sup>1</sup> 

<sup>1</sup>Royal Belgian Institute for Space Aeronomy, Space Physics and STCE, Brussels, Belgium, <sup>2</sup>Center for Space Radiations, ELI-C, Université Catholique de Louvain, Louvain-La-Neuve, Belgium

**Abstract** The Space Weather Integrated Forecasting Framework (SWIFF) Plasmasphere Model (SPM) is a 3D kinetic model of the plasmasphere coupled to the ionosphere. This combined system has been routinely used to evaluate principally the plasmopause formation and evolution, and the plasmasphere's dynamics. The model contains analytical equations for the plasmasphere and plasmatrough regions that have been empirically determined using observations of satellite and ground-based data. In the present work, a revision of the plasmatrough equations is proposed using electron density data from the Van Allen Probes mission and paying particular attention to the spatiotemporal variation as well as to geomagnetic activity influence. Comparisons are performed with other parametrizations and with electron density data from the Arase mission. This assessment demonstrates that the plasmatrough electron density was slightly underestimated with respect to the new observations, in particular for high  $L$  values ( $L > 3$ ) and high geomagnetic activity. In addition, the overall performance of the new parametrization follows a satisfactory general trend despite a large variability of density data observed in the plasmatrough. The plasmatrough is separated from the refilling zone in the model by considering vestigial and outer edge plasmopause positions.

### 1. Introduction

The Earth's plasmasphere is a dynamic toroidal region of cold plasma ( $<1$  eV) that exchanges energy and particles with the ionosphere and the outer magnetosphere (see review book by Darrouzet, De Keyser, et al. [2009] and Darrouzet, Gallagher, et al. [2009]). Between the plasmasphere and the density depleted plasmatrough, an abrupt gradient of plasma density of large variability is named plasmopause (Lemaire & Gringauz, 1998). The whole system is disturbed by geomagnetic storms so that the plasma is eroded and a sharp plasmopause is formed inward from its previous location, expanding the much lower density plasmatrough region beyond. The scenario that has been proposed and confirmed by observations indicates that the plasmopause develops first in the equatorial region at the post-midnight sector (Lemaire & Pierrard, 2008). During periods of increased geomagnetic activity, the plasmasphere is eroded at the nightside. The disturbance evolves with time and induces the formation of density structures, such as shoulders and plumes, in the afternoon and evening sectors (Darrouzet et al., 2008; Darrouzet, De Keyser, et al., 2009; Darrouzet, Gallagher, et al., 2009; Pierrard & Cabrera, 2005; Pierrard & Lemaire, 2004). In addition to the erosion, strongly dependent on the geomagnetic activity history, refilling mechanisms play a complex role in radial and angular variations (Gallagher et al., 2021). During long quiet geomagnetic activity periods, the plasmasphere expands and the plasmopause becomes thicker and with shallower gradient.

Nowadays, there are plenty of models available to simulate the dynamics of the inner magnetosphere using different techniques, with more empirical to more physics-driven assumptions and covering one or several regions together with external and internal boundary conditions (see Pierrard et al., 2009; Reinisch et al., 2009, for reviews of different physics-based and empirical models, respectively). The explosive escalation of machine learning techniques this last decade has enormously contributed to the space environment characterization and, in particular, to the inner magnetosphere investigation. Using ground-based and satellite data to train the statistical systems, it is possible to unravel physical relationships between driven parameters, waves and particles, and to infer density dynamics (Bortnik et al., 2016; Chu et al., 2017; Guo et al., 2021; Zhelavskaya et al., 2017, 2021). It becomes essential for space weather predictions to deepen insight into a more precise description of the plasmatrough dynamics, mainly when depletions lower than  $10 \text{ cm}^{-3}$  provoke enhancements of ultra-relativistic electrons (Alison et al., 2021). The investigation of the plasmatrough is not an easy task since the low density of the plasma

together with the different waves continuously arriving from the outer space, and the particles interacting between themselves and with plasma waves, make difficult the precise evaluation of the spectrum (Kurth et al., 2015).

The Space Weather Integrated Forecasting Framework (SWIFF) Plasmasphere Model (SPM) predicts the density and the temperature of the electrons, protons, and helium ions inside the plasmasphere as well as outside, that is, in the plasmatrough (Pierrard & Stegen, 2008). The model has been coupled to the empirical International Reference Ionosphere (IRI) model (Bilitza, 2018) as boundary condition (Pierrard & Voiculescu, 2011) in the frame of the SWIFF project that allowed the coupling of models for different regions of the magnetosphere (Lapenta et al., 2013). The SPM provides simulations at the ESA SSA (Space Situational Awareness) website (<https://swe.ssa.esa.int/space-radiation>) since January 2017 in a near-real-time basis and for the simulated past dates as a continued and quick assessment of electron density plasmasphere conditions. The plasmasphere and plasmatrough density profiles are simulated in SPM using, basically, the equations for the equatorial density from Carpenter and Anderson (1992) (C&A), extrapolated to cover all the magnetic local time (MLT) sectors and to provide, in addition, simulations over all latitudes. Sheeley et al. (2001) and Denton et al. (2004) have developed statistical models for the plasmasphere and the plasmatrough, with a dependence only in  $L$  and MLT, but, as in C&A, no geomagnetic activity evolution was introduced in such approaches.

The NASA Van Allen Probes mission (Mauk et al., 2013) provided very useful insight to study the inner magnetosphere from the cold plasma to the ultra-relativistic particle populations. Data from this mission have been broadly used to feed empirical models that give the spatiotemporal evolution of the physical problems (De Pascuale et al., 2018; Goldstein et al., 2014; Hudson et al., 2014). More recently, the JAXA Arase mission has arisen to enrich data for the study of wave-particle interactions in the inner magnetosphere (Miyoshi, Shinohara, et al., 2018).

Within this work, the Electric and Magnetic Field Instrument Suite and Integrated Science (EMFISIS) electron density data (Kletzing et al., 2013; Kurth et al., 2015) inferred from measurements performed onboard Van Allen Probes are used to obtain new fitted plasmatrough equations. Both satellites of the mission operated during more than 7 years providing density observations every 6 s. This large amount of data allows obtaining enough statistics for the identification of different dynamical processes with respect to radial and angular variations, and to geomagnetic activity. Indeed, the current investigation aims at feeding the physical equations of the plasmatrough with new observational data in order to assess and improve the simulations in this region. This point has been recently discussed in Pierrard, Botek, et al. (2021) as one of the foreseen improvements to the SPM. The Arase/PWE (Plasma Wave Experiment) plasma dedicated instrument (Kasahara et al., 2018) is used here for further verifications of the new parametrization.

The work is organized in the following sections. Section 2 describes the model and data specifications. Section 3 provides global and particular comparisons between the observations and simulations of the past model version (Pierrard & Voiculescu, 2011) at specific satellite trajectory times and locations. Section 4 shows the data fitting to obtain new improved equations. Section 5 compares the new simulations using these new equations with EMFISIS observations and new independent data from PWE data, as well as with another parametrization. Section 6 shows the influence of refilling in the model and the importance to well identify the external boundary of the plasmopause to clearly separate the external plasmatrough from refilling regions in the observations. Finally, conclusions are delivered about the present implementations and validations in Section 7.

## 2. Model and Database

### 2.1. Model Specifications

The equations defining the plasmasphere region in the SPM have been extensively discussed in Pierrard and Stegen (2008) where the equations defined by C&A in the geomagnetic equatorial plane were used with specific assumptions. The coupling with the ionosphere IRI model is explained in detail in Pierrard and Voiculescu (2011). In this section, we are only explicitly displaying the equations characterizing the plasmatrough, which are the focus of the present investigation. Equations 1–3 are the ones used till now in the SPM to evaluate the electron density ( $N_e$ ) in the plasmatrough in the following MLT intervals:

$$0 \leq \text{MLT} < 6$$

$$N_e = (5,800 + 300 \times \text{MLT}) \times L^{-4.5} + (1 - e^{-(L-2)/10}) \quad (1)$$

$6 \leq \text{MLT} < 15$

$$N_e = (-800 + 1,400 \times \text{MLT}) \times L^{-4.5} + (1 - e^{-(L-2)/10}) \quad (2)$$

$15 \leq \text{MLT} < 24$

$$N_e = ((44,200 - 1,600 \times \text{MLT}) \times L^{-4.5} + (1 - e^{-(L-2)/10})) \times \frac{24 - \text{MLT}}{24 - 15} + (5,800 \times L^{-4.5} + (1 - e^{-(L-2)/10})) \times \frac{\text{MLT} - 15}{24 - 15} \quad (3)$$

Equations 1 and 2 corresponds exactly to the ones defined by Carpenter and Anderson (1992) in the geomagnetic equatorial plane from ISEE satellite and whistler observations. Equation 3 was later inferred to complete the MLT density variation. It can be noticed that the second term of Equation 3 ensures continuity when evolving from  $\text{MLT} = 23$  to  $\text{MLT} = 0$ . The latitudinal variation of the electron density along the magnetic field lines is added in SPM by means of the following equation based on a dipole dependence (see Denton et al., 2006):

$$N_{e_\lambda} = N_e \times \cos^{-2\alpha}(\lambda) \quad (4)$$

where  $\lambda$  is the magnetic latitude and  $\alpha = 2$  for the plasmatrough region. Indeed, Denton et al. (2006) considered such value as a general result from previous investigations since it represents an intermediate between the dependence expected for diffusive equilibrium and so called collisionless models for the steeper low-density plasmatrough. Equations 1–4 will be noted C&A\* all over this work. The electron density will be named simply  $N_e$  even if the latitudinal variational is considered.

Before determining the cold plasma density in the different regions of the inner magnetosphere (plasmasphere and plasmatrough), the SPM calculates the plasmopause location using the mechanism of interchange instability (Pierrard & Lemaire, 2004). The SPM simulations using this approach have been extensively validated against observations. See for example, Verbanac et al. (2018). In addition, the SPM has been recently improved to provide at least one plasmopause point at every 1-hr-MLT sector, in particular during stormy times for sectors involving the evening and night local times. A dynamic interpolation procedure has been implemented to settle any missing information. An accurate evaluation of the plasmopause borders is the essential departing point to better simulate the plasmasphere and plasmatrough regions. This task remains very difficult in the sectors with plumes, but the procedure seems successful in a global basis, and it is already implemented for use in all the future simulations performed with the model.

After the plasmopause location ( $L_{pp}$ ) is evaluated, the corresponding C&A equations for the plasmasphere and the plasmatrough are employed for regions where  $L < L_{pp}$  and  $L > L_{pp}$ , respectively.

## 2.2. Database Specifications

The Van Allen Probes, previously called Radiation Belts Storm Probes (RBSP), were a mission of two spacecraft (A and B) in tandem following a highly elliptic orbit with a perigee of 618 km and an apogee of 30,414 km. The orbit presented  $10^\circ$  of inclination with respect to the magnetic equator and a period of around 9 hr (Mauk et al., 2013). The twin satellites were launched in 2012 and were decommissioned in 2019. Onboard, the EM-FISIS instrument provided the upper hybrid resonance frequency from which the electron density was inferred (Kurth et al., 2015). Such procedure required some manual intervention especially during nonquiet periods when the spectra became complex. There are two sources of error in the determination of electron densities from the plasma wave spectrum: (a) the spectral resolution of the instrument, which translates to a density resolution of about 10% and (b) the interpretation of the plasma wave spectrum that could induce much larger errors (see Kurth et al., 2015 for details). Indeed, the low plasmatrough densities remain the most complex to infer, especially during geomagnetically active periods. Since there are several banded emissions observed in this region, the determination of density requires more particular assumptions and manual inspections to correct the procedure. In addition, we have filtered out values  $>2,000 \text{ cm}^{-3}$  due to the limited response above 400 kHz of the instrument (Kletzing et al., 2013; Kurth et al., 2015). The lowest detection limit of the instrument was 10 kHz corresponding to a density of  $\sim 1 \text{ cm}^{-3}$ . Data from both spacecraft are used here for the statistics.

The Arase mission, formerly known as Exploration of energization and Radiation in Geospace (ERG), was launched in December 2016 in a highly elliptic orbit with a perigee of 460 km, an apogee of 32,110 km and an inclination of  $31^\circ$ . The period is also around 9 hr (Miyoshi, Shinohara, et al., 2018). The local electron density data are derived from the frequency spectra determined by the High Frequency Analyzer (HFA; Kumamoto et al., 2018) subsystem, which is part of the PWE (Kasahara et al., 2018), and using the local magnetic field measured by the Magnetic Field Experiment (MGF; Kasahara et al., 2021; Matsuoka et al., 2018). A semiautomated procedure to derive the electron density has been also developed with an average error rate below 7.8% when the wave frequency is above 30 kHz and when the wave spectral intensity is less than  $10^{-5}$  mV<sup>2</sup>/m<sup>2</sup>/Hz (Matsuda et al., 2020). More sophisticated techniques from deep learning without additional features based on expert knowledge allow to determine the upper hybrid frequency and, thus, the electron density with high accuracy (Hasegawa et al., 2019).

### 3. Comparisons Between EMFISIS Observations and SPM Simulations

Once the ephemeris and density data were retrieved for the whole period of the mission and for both satellites, the data were resampled from 6 s to 1 min. Then, the satellite trajectory data every 30 min (at 00 and 30 min of each hour) were extracted and used as input for simulations of the SPM model, together with the Kp indices corresponding to the simulation day and to the precedent one. The Kp index data (Matzka et al., 2021) were also merged to the whole final table of observations and simulations variables in order to perform further filters for different geomagnetic activity periods.

A systematic and global analysis of the correlation between EMFISIS data and SPM simulations (with the C&A\* parametrization) of the electron density in logarithmic scale is displayed in Figure 1 for ephemeris every 30 min and split into three Kp periods, quiet ( $K_p < 3$ ), moderate ( $3 \leq K_p < 5$ ), and stormy ( $K_p \geq 5$ ) times and into four MLT sectors each containing six MLT hours. The color scale corresponds to the *L*-parameter (McIlwain, 1966). SC is the Spearman Coefficient (Bonett & Wright, 2000) and RMSE is the root mean square error evaluated using the logarithmic values.

The plots put in evidence the two different regions modeled by two different sets of equations and separated by the plasmapause boundary: the plasmasphere at lower *L* with higher densities and the plasmatrough at higher *L* with lower densities. At the extreme of high densities, there is a better correlation between observations and simulations since the data are close to the diagonal black line. At low densities, correlations are worse.

Very large deviations are observed at the boundary zone where a sharp transition is ruled by the fitting. At this zone, the plasmasphere equations (Carpenter & Anderson, 1992) generate values progressively overestimated by 1–2 orders of magnitude when *L* increases and, inversely, the plasmatrough equations underestimate the observations by 1–2 orders of magnitude for decreasing *L*. Looking at the different plots in Figure 1, no specific correlations can be disentangled between the density variability and Kp or MLT. The sample sets for the Kp ranges  $\geq 3$  are perhaps too limited to draw strong statistical conclusions, in particular for  $K_p > 5$ ,  $MLT = 0-6$ . One can also see that the observations in the plasmatrough are very variable in all MLT and for  $K_p < 5$ , as disclosed by the almost horizontal distribution of the red symbols at high *L* in Figure 1. This shows that any statistical model driven by indices such as Kp, or by any other empirically derived average inputs, will always have difficulties to reproduce each individual observation in this region, except if the dynamic processes implicated in these variations can be well understood.

Figure 2 displays the electron density for RBSP-A in 2015–2016 as a function of *L* for a particular Kp range ( $< 3$ ) and a particular MLT sector (9–15) as an example that considers only calm periods during the day local times (without any formation of plumes or shoulders). Indeed, as noticed more clearly in Figure 2, the observation points (in red), even if gathered in two regions, are more dispersed in-between the two regions than the corresponding simulations (in green), which concentrate more around their C&A\* fitting curves.

We have considered a sharp plasmapause in the present simulations. Refilling can be also taken into account in the simulations of the SPM model when analyzing specific cases (Pierrard & Stegen, 2008), but it has not yet been included in an automatic way and is thus not included in Figures 1 and 2 (see Section 6 of the present article for more details). In the present long-term SPM simulations, the plasmasphere is thus always sharply separated from the plasmatrough by a simple plasmapause boundary, without taking into account the thickness of this layer, the refilling time or the plasmaspheric wind (Pierrard, Botek, et al., 2021), which could dramatically change the

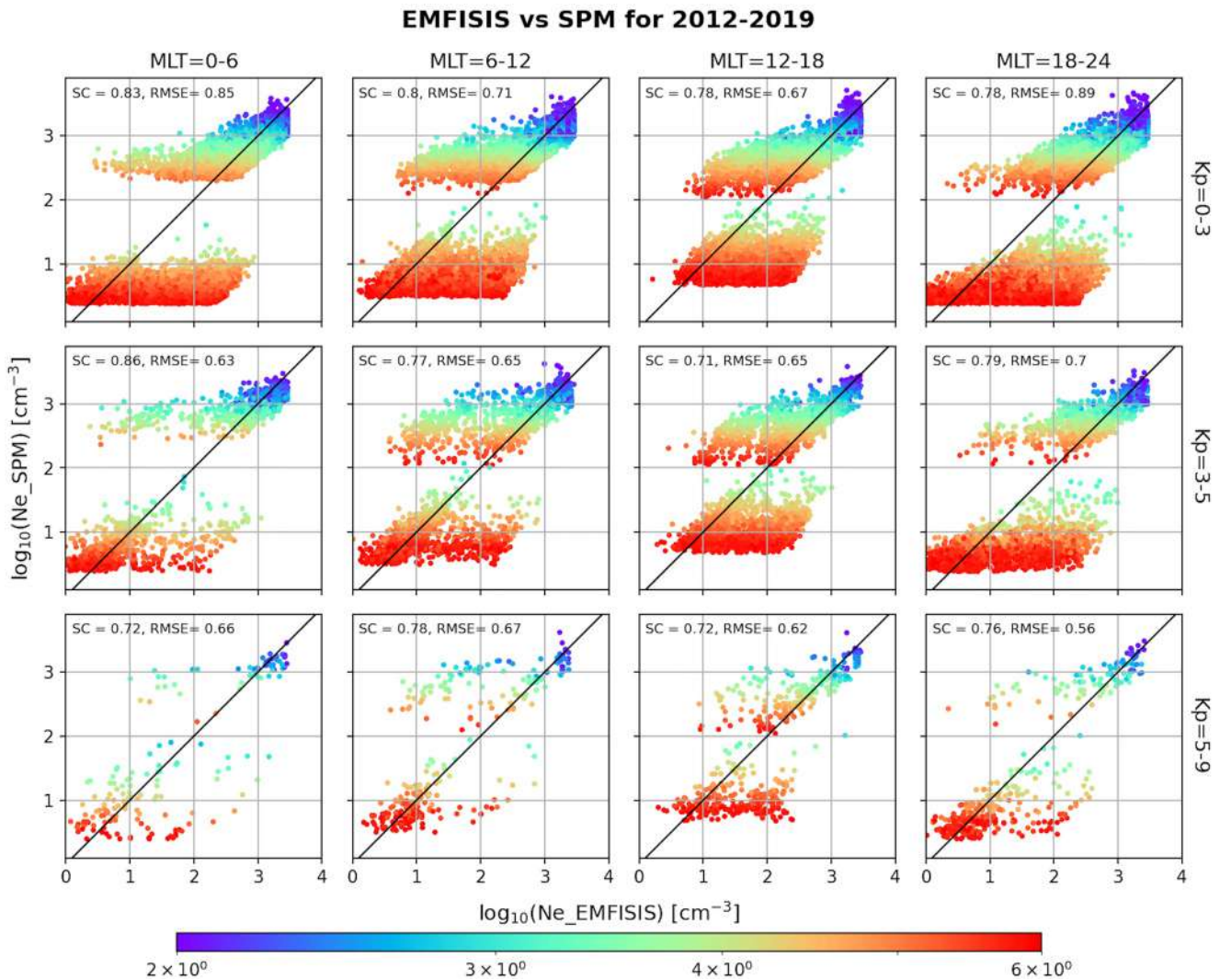


**Figure 1.** Logarithm of the Plasmasphere Model (SPM) simulated densities at locations of the Radiation Belts Storm Probes (RBSP)-A and RBSP-B spacecraft as a function of the logarithm of the corresponding electron densities determined by Electric and Magnetic Field Instrument Suite and Integrated Science (EMFISIS) for four different magnetic local time (MLT) sectors (columns) and three different Kp ranges (rows). The black diagonal line indicates where the model densities exactly correspond to the observed values. The color scale corresponds to the McIlwain parameter  $L$ . SC, the Spearman Coefficient and RMSE, the root mean square error, are provided at the top of each panel, both evaluated using the logarithmic values.

density evaluated at the plasmatrough. That is why Figure 2 does not show any transition region between the plasmasphere and the plasmatrough for the SPM values (in green).

The high RMSEs in the figures are due to these significant deviations. Moreover, approximating the plasmatrough as the region where  $N_e < 100 \text{ cm}^{-3}$ , it can be seen that the simulated points of Figure 2 globally underestimate the corresponding observations.

#### 4. Using EMFISIS-Fitted Data in the SPM Model

We focus here on improving the plasmatrough Equations 1–3 of the model since simulations of waves generated in this region of the inner magnetosphere need precise density estimations (Pierrard, Ripoll, et al., 2021) and they present severe deviations when compared to EMFISIS data. The plasmapause locations ( $L_{pp}$ ), obtained with SPM as explained in Section 2.1, were averaged for each MLT hour and used as reference to identify the plasmatrough points in the EMFISIS data ranged from 2012 to 2019 and resampled to 5 min. The observations with  $L > L_{pp}$  were then retained. The electron densities were then projected on the magnetic equator using Equa-

**RBSP-A/EMFISIS (red) vs SPM (green) for kp=0-3 MLT=9-15 in 2015-2016**  
SpearmanCoeff= 0.76, RMSE= 0.65

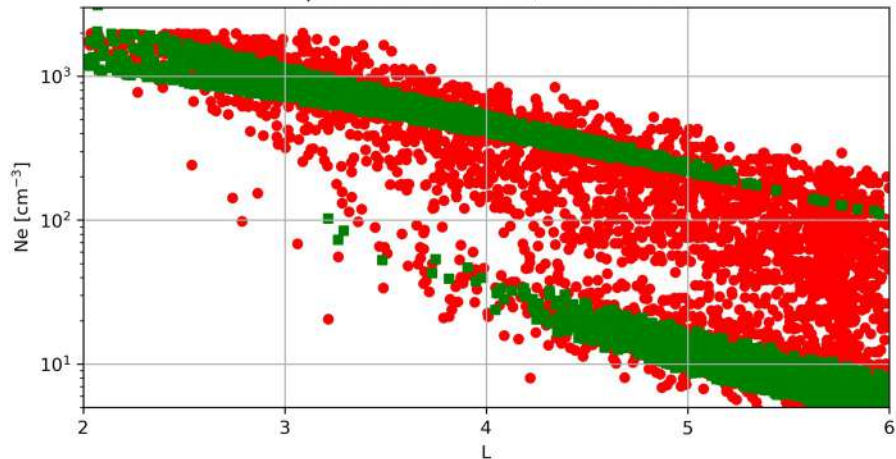


**Figure 2.** Electron densities given by RBSP-A/Electric and Magnetic Field Instrument Suite and Integrated Science (EMFISIS) data (red) and the SPM simulations (green) at locations of the spacecraft every 30 min in 2015–2016 for Kp < 3 and magnetic local time (MLT) between 9 and 15 hr. The Spearman Coefficient and RMSE (root mean square error) are also displayed.

tion 4 for the corresponding latitudes to obtain the equatorial  $N_e$  values. The measurements took place mostly at low latitudes as the inclination of the orbit of the RBSP satellites was  $10^\circ$ . The resulting data were also binned as follows: 24 bins of 1 hr for MLT and 40 bins of  $0.1 R_E$  from 2 to  $6 R_E$  for  $L$ . The data were also split into quiet ( $K_p < 3$ ) and (sub)stormy ( $K_p \geq 3$ ) periods, since the density decrease is clearly very different in these two

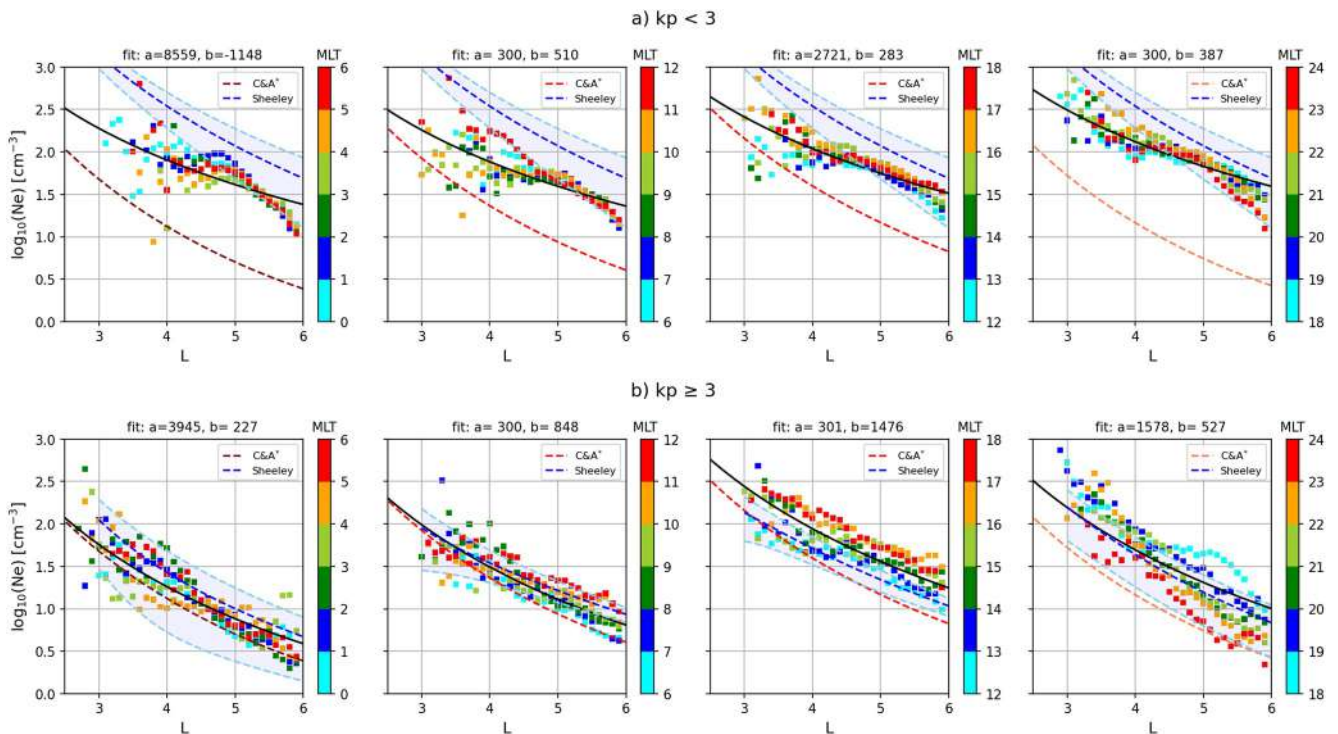


**Figure 3.** Plasmatrough electron density determined by Electric and Magnetic Field Instrument Suite and Integrated Science from 2012 to 2019 in the range  $L = 2-6$  ( $R_E$ ) and fitted by new equations for different magnetic local time (MLT) sectors and for two different Kp regimes: (a)  $K_p < 3$  and (b)  $K_p \geq 3$ . Solid black lines represent the new fit using Equation 5. Dashed red lines display the fits given by previous Equations 1–3 by C&A\*. Dashed blue lines delimit the regions covered by the equations of Sheeley et al. (2001) for the plasmasphere in (a) and for the plasmatrough in (b). All the dashed lines are evaluated at the middle (MLT + 3) of the corresponding MLT sector containing six MLT hours for MLT-dependent equations.

regimes, as illustrated in Figures 3a and 3b, respectively, displaying four panels with different MLT sectors for each Kp regime. Each panel, containing data from six MLT hours, gathers observations bins in each MLT hour, easily identified by a specific color to display the MLT variability of the scatter points in the respective region.

The reddish dashed lines in Figure 3 represent Equations 1–3 used in the SPM model (C&A\*) in three different red tones according to the MLT range. The light blue dashed lines indicate the deviation limits proposed by Sheeley et al. (2001) (the darker blue line being the main equation), inside the plasmasphere in Figure 3a and in the plasmatrrough in Figure 3b. Both the C&A\* and Sheeley’s curves were calculated at “MLT + 3” in each range containing six MLT hours in Figure 3.

Based on the C&A\* equations as a function of  $L$  and MLT, a new fitting was performed for the four 6-hr-MLT sectors, by using the following equation to describe the equatorial electron density in the plasmatrrough:

$$N_e = (a + b \times (\text{MLT} + 3)) \times L^c + (1 - e^{-(L-2)/10}) \quad (5)$$

where MLT takes the values: 0, 6, 12, 18, so that “MLT + 3” locates at the middle of the six MLT’s group when the fit is performed.

In a preliminary step, a series of fitting tests using Equation 5 was thus conducted to inspect the global data variability, and, finally, a fixed value was assigned to  $c$  parameter in each Kp regime for all four MLT ranges. Therefore,  $c$  was set to  $-3$  for  $K_p < 3$  and to  $-4$  for  $K_p \geq 3$  for the four MLT ranges. These values assigned to  $c$  correspond to the ones fitted for the MLT = 0–6 sector in each Kp regime. This MLT period includes the local times where the plasmopause is created and the observations distribution matches better the regions covered by other previous approximations like the one proposed by Sheeley et al. (2001). This choice permits to adjust the progressive quicker decay of the density evolution with  $L$  values for increasing stormy times, as well as to ensure a physical continuity of density distribution in simulations. After fixing  $c$ , only  $a$  and  $b$  were free parameters, and the corresponding fitted equation is displayed as a solid black line in both Kp regimes of Figure 3.

The lines corresponding to the C&A\* equations of the model are in general located lower than the ones obtained from EMFISIS data, in particular for higher  $L$ , and with a quicker and unique decrease  $-4.5$  factor everywhere in C&A\* (see Figure 3). Since the low Kp profiles are so different and could be due mainly to plasmaspheric extension, only the fitting parameter sets for  $K_p \geq 3$  regime are used in the model to test the new version of the plasmatrrough equations. Indeed, for more quiet geomagnetic times ( $K_p < 3$ ), the plasmasphere is expanded to higher  $L$ , even to  $L > 6$ . Accordingly, the observational data displayed in the top panels of Figure 3 for  $L > 4$ , and with densities 1 order of magnitude larger than those of the plasmatrrough from C&A\* and Sheeley’s curves, could correspond better to plasmaspheric zones due to relaxation instead of plasmatrrough densities. In order to assess this assumption, the equations for the plasmasphere density from Sheeley et al. (2001) are displayed in (a) instead of the ones for the plasmatrrough, but only the lower part of Sheeley’s confidence region overlaps the new curve for  $L > 4.5$  demonstrating, so far, the limits of the present approximations to describe the dynamics between the plasmasphere and the plasmatrrough. On the other hand, data for  $K_p \geq 3$  seem to better describe the plasmatrrough region. Indeed, the new fitting remains in general inside the plasmatrrough Sheeley’s ranges but accounts for a slower variation of  $N_e$  with  $L$  than that of C&A\* and more consistent with Sheeley’s curves, in particular for 0–6 and 6–12 MLT ranges. The  $K_p \geq 3$  equations will then generate a larger correction of the plasmatrrough density at higher  $L$  for MLT = 0–12 and nearly over the whole  $L$  range for MLT = 12–24. Also note the trough midnight to dusk rise in density that is observed with EMFISIS and can be associated with refilling from the ionosphere, and the post dusk reduction in trough density observed in the first panel of Figure 3.

Another feature of the  $K_p \geq 3$  subplots in Figure 3b is the larger deviation of the EMFISIS observational data for the MLT = 12–18 region (Figure 3b, third panel) and  $L > 4$  from the area covered by all the parametrizations. This substantial deviation toward higher densities can be explained by the formation of plumes that occurs at MLT around 15 hr for nonquiet periods as well illustrated in Figure 4. This Figure 4 displays the EMFISIS equatorial densities binned in  $L$ –MLT where the color scale represents the mean logarithmic density of each bin. The relaxed plasmasphere extends everywhere to higher  $L$  in less active times (left panel), whereas the middle and right panels capture the plume patterns during more active periods. Indeed, there are statistically more plumes in the afternoon sector (Darrouzet et al., 2008), which supports the density increase around MLT = 15. These plumes rotate with the Earth, but such rotation cannot be appreciated here since each of these plots represents a static feature merging all the possible measurements during the whole period of Van Allen Probes. This is,

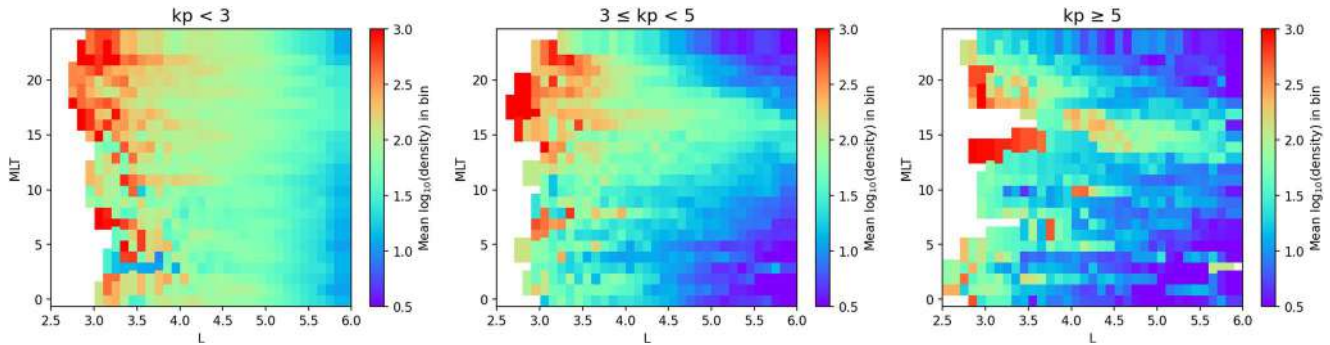


**Figure 4.** Split of the magnetic local time (MLT)– $L$  binned logarithmic plasmatrough equatorial Electric and Magnetic Field Instrument Suite and Integrated Science electron density in  $\text{cm}^{-3}$  for three Kp regimes showing a more relaxed plasmasphere over higher  $L$  for  $Kp < 3$  (left panel) and the plumes region extension for  $Kp \geq 3$  (middle and right panels) around  $MLT = 15$ .

however, a useful mapping to visualize the whole range of observations. The plasmaspheric higher densities are extended inside the plumes, but the densities are significantly lower all over the other MLT sectors by the plasmasphere erosion during more stormy times. Such effect supports the choices done for the fitting procedure.

Finally, the fitting parameters obtained with the EMFISIS density data split in the four different MLT sectors and during the periods of larger geomagnetic disturbance ( $Kp \geq 3$ ) have been chosen to improve the plasmatrough semiempirical relations. They take into account the dynamical phenomena that impact the plasmatrough density for different radial and angular variations and ensures the real physical continuity of the mass density. This new parametrization will be named EMFISIS-fitted from now on in the article. The general equation used in the model for the calculation of any 3D point of the plasmatrough density to smooth unphysical discontinuities as much as possible between MLT subsectors has the following form:

$$N_e = \left( (a + b \times MLT) \times L^{-4} + (1 - e^{-(L-2./10)}) \right) \times \frac{m_{lt2} - MLT}{m_{lt2} - m_{lt1}} + \left( (a' + b' \times MLT) \times L^{-4} + (1 - e^{-(L-2./10)}) \right) \times \frac{MLT - m_{lt1}}{m_{lt2} - m_{lt1}} \quad (6)$$

where  $m_{lt1}$  and  $m_{lt2}$  correspond to the limits of the four MLT sectors: 0–6, 6–12, 12–18, and 18–24 and ( $a'$ ,  $b'$ ) correspond to the fitting parameters of a sector consecutive to a sector with ( $a$ ,  $b$ ) parameters following increasing local times. When  $MLT \geq 18$ , then  $b'$  is set to 0 to ensure continuity when passing from  $MLT = 23$  to  $MLT = 0$ . The latitudinal dependence is also considered for the 3D variation along the magnetic field lines of a dipole as in Equation 4.

New simulations were then performed with the model using these new fitting equations. Comparisons between the simulated (EMFISIS-fitted) and observed values during a short period spanning March 2015, which includes the day of the Saint Patrick storm (March 17), are taken as example. They are displayed in Figure 5 by means of time series of the ratio between the logarithmic density of the simulations and the logarithmic density of the observations (black crosses) for two  $L$  zones to explore the model performance in the plasmasphere and in the plasmatrough, approximately represented by lower  $L$  (top panel) and higher  $L$  (middle panel), respectively. Comparison is also displayed on both panels with the C&A\* parametrization (red dots).

Deviations are substantially smaller for lower  $L$  (top panel) and for more quiet times, corresponding to a more extended plasmasphere. It should be noted that the correction with EMFISIS data is not expected in this region, where the equations of C&A corresponding to the plasmasphere zone are valid and have not been modified. Hence, the red dots and black crosses overlap nearly everywhere with rare exceptions of some points corresponding to the plasmatrough region near the plasmopause during nonquiet times. When the geomagnetic activity increases, the correlation is less good at low  $L$  (points deviate more from 1) indicating a perturbed plasmasphere as observed between 17 and 18 March 2015. On the contrary, the correlation is bad everywhere for higher  $L$  (middle panel) and becomes still worse for stronger geomagnetic activity, demonstrating the limits of the model to reproduce EMFISIS observations of the plasmatrough, even when the new parametrization is applied (EMFISIS-fitted, black crosses). The statistical scores confirm the better performance of the model in the plasmasphere with quite low RMSE, which anyway is still mildly impacted by the (sub)stormy times. For higher  $L$ , the RMSE is substantially larger but is improved by the introduction of the new plasmatrough parametrization, as reflected by a decreased RMSE from 75% for the C&A\* parametrization



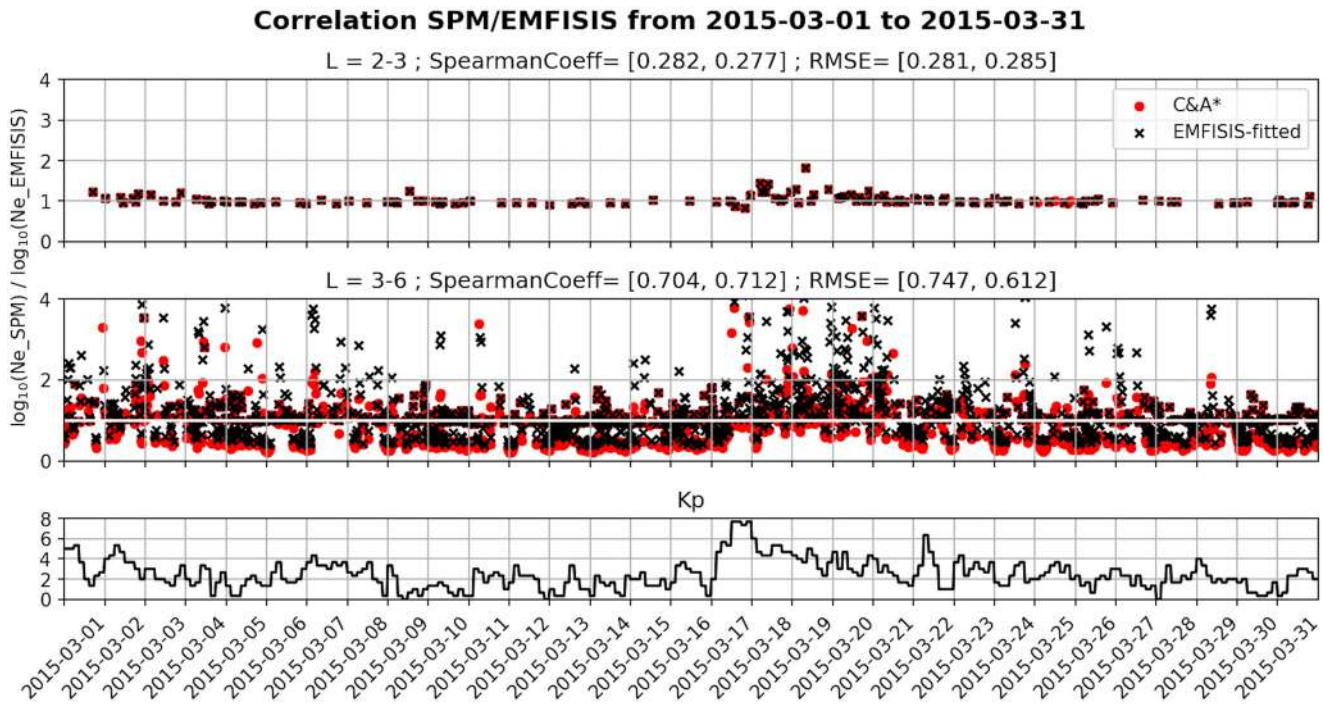


**Figure 5.** Ratio between the  $\log_{10}$  of the simulated and the  $\log_{10}$  of the Electric and Magnetic Field Instrument Suite and Integrated Science (EMFISIS) observed electron density in March 2015 for two regions of  $L$ :  $L = 2-3$  (top panel) and  $L = 3-6$  (middle panel) for C&A\* parametrization (red dots) and the new EMFISIS-fitted parametrization (black crosses). The Spearman Coefficient and the RMSE are displayed for C&A\* parametrization (left) and for the new EMFISIS-fitted parametrization (right). The Kp variation is added for the whole period in the bottom panel.

(first number in the title of the middle panel) to 61% for the EMFISIS-fitted parametrization (second number) at higher  $L$  (red points are often lower than 1 while black ones are often closer to 1). The SC is rather weak for series correlation at lower  $L$ , but it becomes stronger for higher  $L$  series, mainly due to many simulated points that systematically remain undervalued in comparison to observations. It can be also observed that for  $L > 3$  during quiet periods (as e.g., between March 8 and 16), the deviation of the simulations remains significantly lower (closer to 1) than during more disturbed times (March 16–21), which also justify the use of the new parametrization.

Figure 6 compares the output of the model in the equatorial and meridian views for the version using the C&A\* parametrization (left panels) and for the version using the EMFISIS-fitted parametrization (right panels) during the Saint Patrick storm in 2015. The plasmapause is represented by the small black empty circles in the equatorial view. The density color scale is saturated in these plots for the plasmasphere region in order to better see the

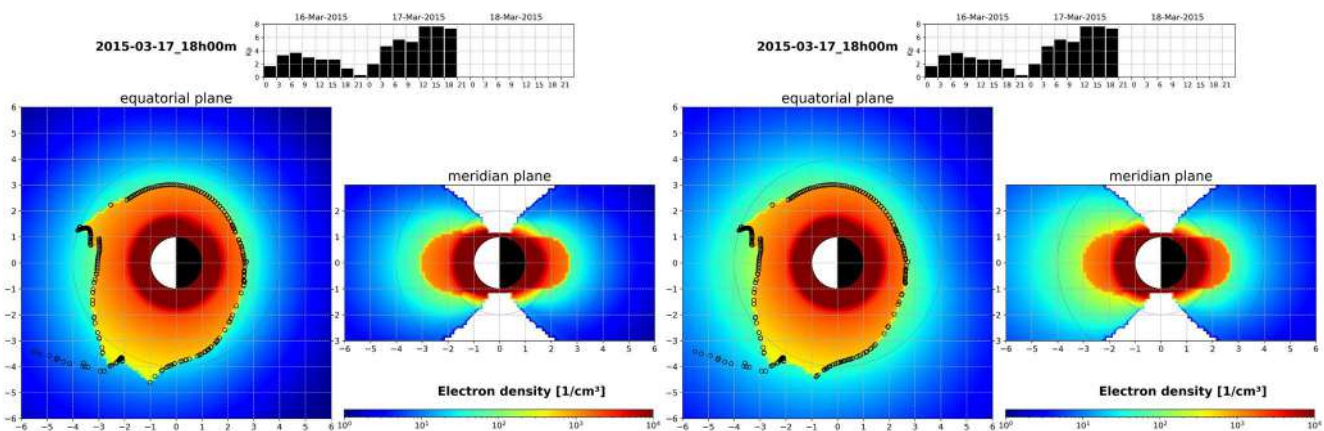


**Figure 6.** Equatorial and meridian simulation views of stormy times using Equations 1–3 with C&A\* parametrization in left panels and using Equation 6 with Electric and Magnetic Field Instrument Suite and Integrated Science-fitted parametrization in right ones.

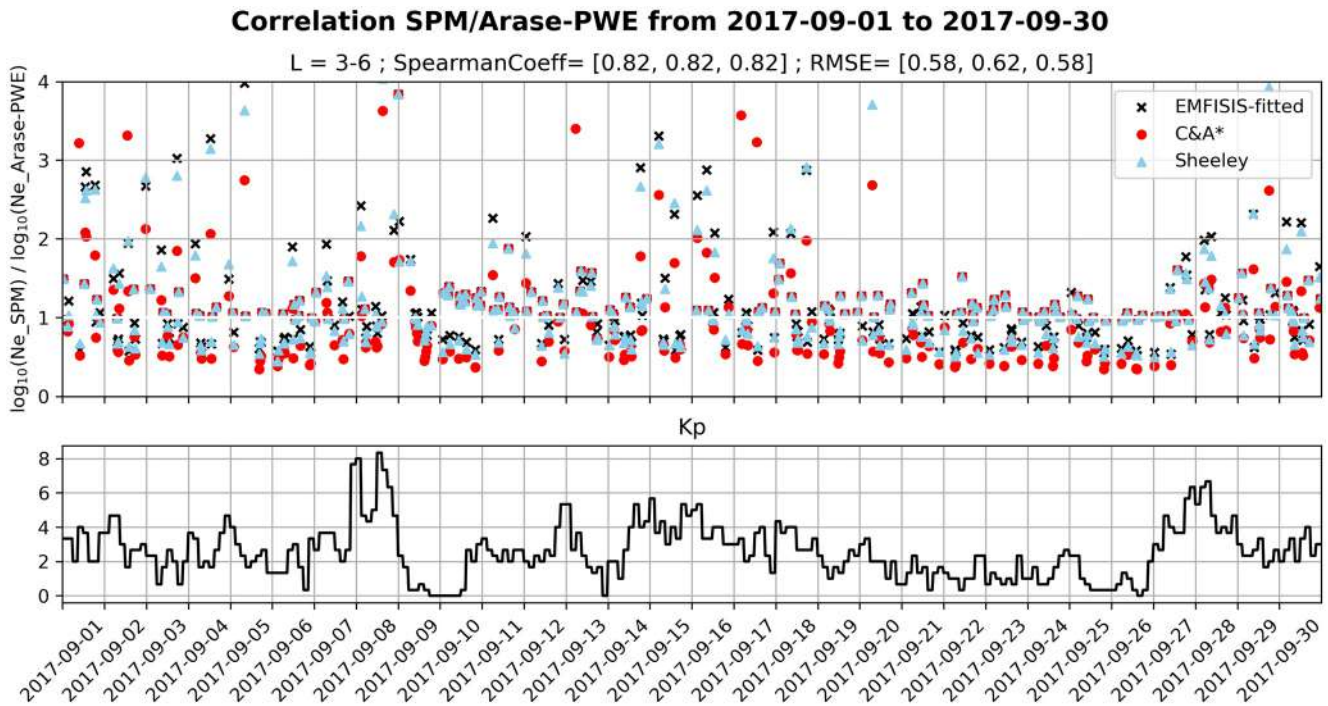


**Figure 7.** Top panel: ratio between  $\log_{10}(\text{Ne\_SPM})$  and  $\log_{10}(\text{Ne\_Arase-PWE})$  for September 2017 and for  $L = 3-6$ . Three series of results are displayed for simulations with SPM involving different parametrizations of the plasmatrough: Electric and Magnetic Field Instrument Suite and Integrated Science (EMFISIS)-fitted (black crosses), C&A\* (red dots), and Sheeley (blue triangles). Spearman Coefficients and RMSE are shown for each parametrization in comparison with the satellite data in the mentioned order. Bottom panel:  $K_p$  evolution during this period (September 2017).

differences in the plasmatrough between the old and the new parametrizations (yellow-green-blue region). Concerning the plasmatrough density, the plots on the right displaying the new EMFISIS-fitted parametrization show a density slightly higher than in the previous plasmatrough model (C&A\* parametrization on the left), in line with the curve trend obtained in Figure 3b. During this stormy period,  $K_p$  increases and the plasmasphere is eroded. After the storm,  $K_p$  decreases, so that the new plasmapause is located further than during the storm. In such cases, refilling will take place in the regions that were eroded during the storm. This refilling was not taken into account until now in this article, while it plays an important role in the model to reproduce intermediate densities between the saturated plasmaspheric flux tubes and the low-density plasmatrough (see Section 6 for further discussion).

## 5. Comparison With Arase/PWE Density Data

The ratios between the logarithm of simulations and the logarithm of observations at  $L = 3-6$  are displayed in Figure 7 for September 2017 using the SPM code and the Arase/PWE density data. The SPM plasmatrough evaluations encompass here three parametrizations: EMFISIS-fitted (black), C&A\* (red), and Sheeley (blue). The SC and RMSE scores are indicated for the three series of comparisons demonstrating their similar performances, without significant improvement of the new parametrization (EMFISIS-fitted). C&A\* appears to provide systematically slightly lower ratios than the latter and Sheeley's, but the performance of this model is not better than the others because the ratios are often lower than 1 during quiet periods. The calm period between September 18 and 26 demonstrates a better reproducibility of observations from the three series of parametrizations than during disturbed periods. The similarity between all these series of data and the large variability encountered also in Arase/PWE observations point out once more the challenge of describing the plasmatrough with averaged empirical relations depending on  $L$ , MLT, and  $K_p$ .

## 6. Refilling

Because we were mainly interested by the improvement of the plasmatrough region, up to now we have considered only the equations of the saturated density profiles in the SPM, leading thus to only two very different

regions, one inside the plasmapause and one outside, the plasmatrough, as clearly illustrated in Figure 2. Nevertheless, nonsaturated profiles can also be considered in the model (Pierrard & Lemaire, 2001). They mainly appear after geomagnetic storms when the magnetic flux tubes refill after the plasmaspheric erosion. This should yield the intermediate points that are observed in Figure 2 with EMFISIS density data (in red) between the two modeled profiles (in green) corresponding to the saturated plasmasphere and the plasmatrough.

To take into account this refilling appearing mainly during decreasing phases of Kp, we consider, in addition to the present modeled plasmapause obtained with the model 24 hr before the current date, the vestigial plasmapause obtained for the previous day as already explained in Pierrard and Stegen (2008). When Kp decreases, this vestigial plasmapause is located at lower distances, at least for some MLT sectors, and refilling takes place between this vestigial plasmapause and the new one appearing at larger distances.

The views of the top panel in Figure 8 illustrate the plasma density 9 days after the strong Saint Patrick storm in 2015. In the bottom panel, the Kp evolution from the Saint Patrick Day and during 10 days after is displayed to

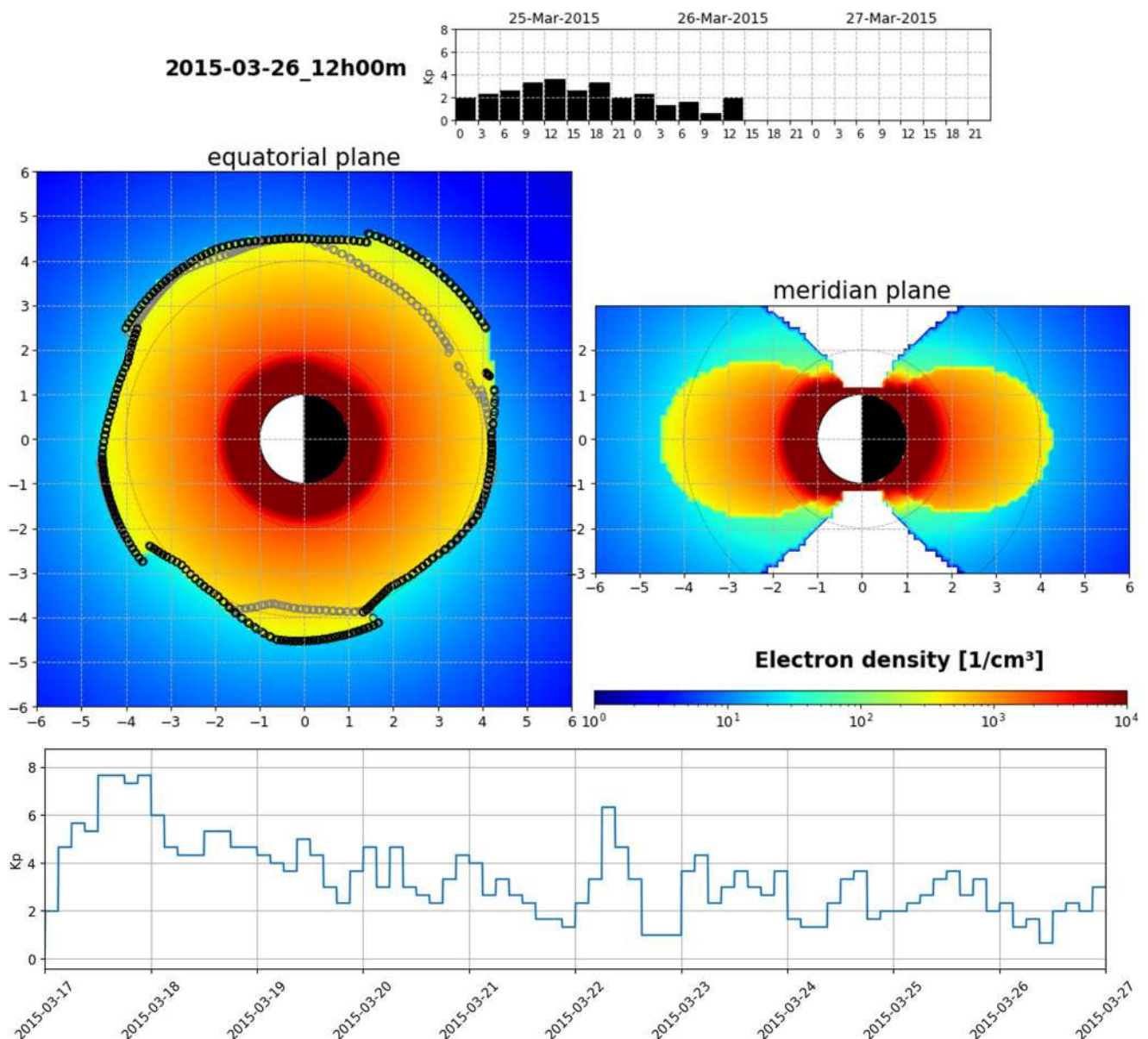


**Figure 8.** Top panels: plasmasphere recovering after storm with previous 24 hr vestigial plasmapause (gray empty circles) and current plasmapause (black empty circles) displayed in the equatorial plane (left) and in the meridian plane (right). Bottom panel: 10 days of Kp from the Saint Patrick storm in 2015.

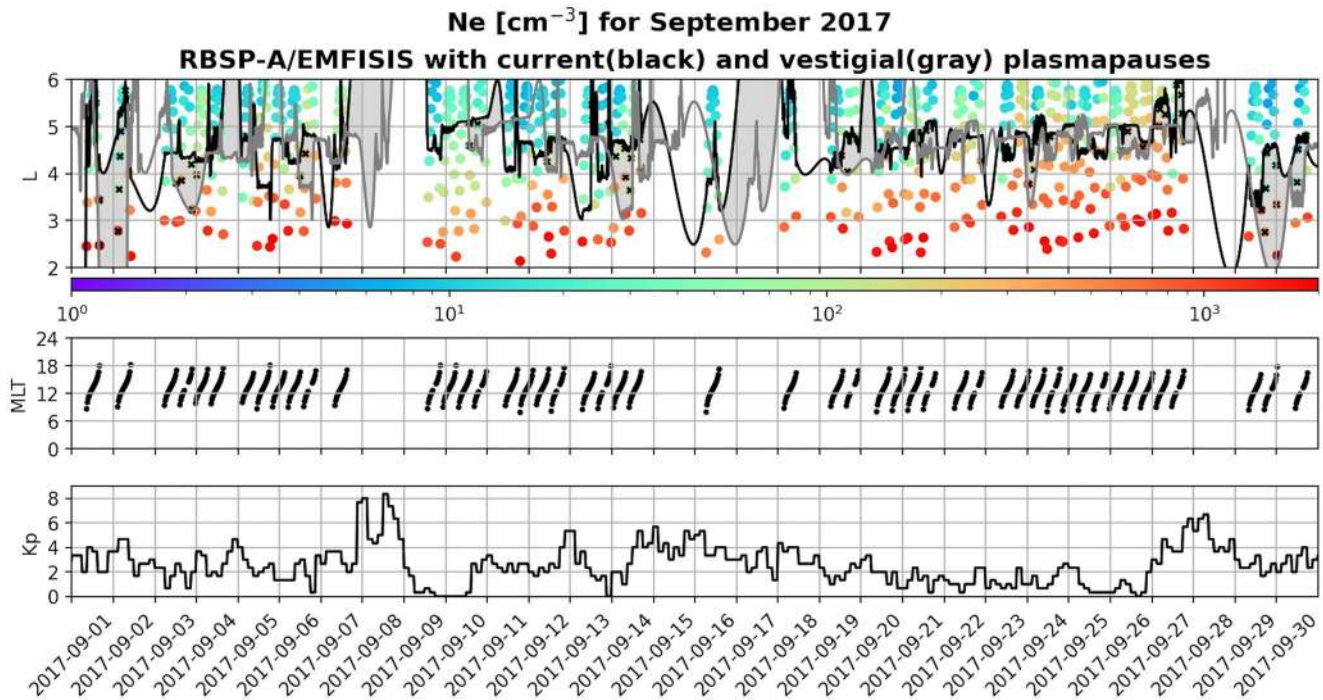


**Figure 9.** Top panel: Electric and Magnetic Field Instrument Suite and Integrated Science (EMFISIS) density data ( $\text{cm}^{-3}$ ) observed along the trajectory of RBSP-A during September 2017 with the  $L$  distribution in the vertical axis. The current (in black) and vestigial (in gray) plasmapause locations ( $L_{pp}$ ) evaluated using SPM are plotted. The gray dressings correspond to refilling regions and the observations confined inside them have been highlighted with black crosses. Middle panel: magnetic local time (MLT) of the EMFISIS observations. Bottom panel:  $K_p$  evolution during the period.

illustrate the geomagnetic activity. The plasmasphere is recovering/relaxing from a period of strong activity. The equatorial view (left top panel) displays not only the current plasmopause (black empty circles) but also the vestigial plasmopause (gray empty circles) that was formed during the previous 24 hr with an inner magnetosphere exposed to more enhanced geomagnetic activity during the previous 48 hr. Hence, the simulation takes into account these 2 days where the vestigial plasmopause represents the inner edge of the plasmasphere boundary layer (concept first introduced by Carpenter & Lemaire, 2004) and the current plasmopause represents the outer edge. During this recovery period, when the  $K_p$  is decreased, the plasmopause is less sharp than during periods of strong activity and it becomes a thicker boundary layer between inner and outer edges where refilling takes place. This dynamical extension of the plasmopause region could explain the large distribution of observational density points at high  $L$ , which are neither reproduced by the equations of the saturated density profiles of the plasmasphere nor by those of the plasmatrrough in Figure 2.

To this end, Figure 9 illustrates the proposed approach using EMFISIS observations for September 2017. In the top panel, the observed density is plotted as dots at the locations of RBSP-A displaying the radial variations along the time. The satellite trajectory MLT values and the corresponding  $K_p$  indices are also displayed at the middle and bottom panels, respectively. The current (in black) and vestigial (in gray) plasmapauses obtained with SPM are superposed in the top panel. The region between both plasmapauses is filled with gray when refilling takes place, that is, when the plasmopause from the previous day is closer to the Earth than the current one. The observations remaining inside such refilling region are marked with black crosses and they are also represented in Figure 10. In Figure 10, the correlation between the observations for the same period of Figure 9 and the corresponding simulations from SPM (EMFISIS-fitted) is displayed. It can be noticed that many of the black crosses imply observations located in-between the plasmasphere and the plasmatrrough simulated points, confirming that refilling plays an important role to represent the intermediate densities between the saturated plasmasphere and the plasmatrrough limits. The refilling rate could be then evaluated from the EMFISIS observations using this procedure automatically. Up to now, the thickness of the plasmopause and the refilling process using SPM can be performed only for case studies considering manually the two different edges of the plasmopause. Further improvements to the model will involve the automatic consideration of the vestigial inner border of the plasma-

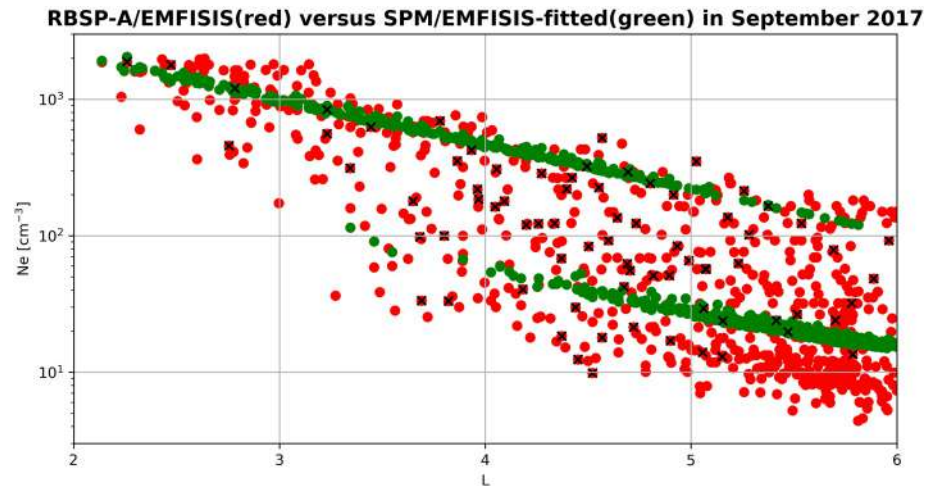


**Figure 10.** RBSP-A/Electric and Magnetic Field Instrument Suite and Integrated Science (EMFISIS) observations (red) versus SPM/EMFISIS-fitted simulations (green) in September 2017. Black crosses highlight the corresponding observations inside the gray regions as in Figure 9 top panel.

pause when the geomagnetical activity is diminished, and, thus, a thicker zone delimiting the plasmasphere and plasmatrough. The density in this zone should evolve in a progressive basis to better reproduce the observation trends in the region between the plasmasphere and the plasmatrough at large distance.

## 7. Conclusions

The plasma electron density evaluated by the SPM 3D dynamic model of the plasmasphere and plasmatrough has been assessed by implementing a new parametrization based on observational data from RBSP/EMFISIS instrument and compared with Sheeley parametrization and Arase/PWE data. The attention was dedicated to the plasmatrough region, which has been less addressed in previous investigations, where the plasmasphere region was the principal objective due to its much higher densities and to its strong interaction with the ionosphere (as e.g., in Lapenta et al., 2013) and the radiation belts (Darrouzet et al., 2013). In addition, future use of SPM in combined implementations with other models of the inner magnetosphere requires a verified performance of the model all over the cold plasma region.

As a general estimation, the parametrization obtained with EMFISIS data provides a less sharp variation of the plasmatrough density from the plasmopause location outwards. The large variability and high dynamics of such low-density data make difficult the decrease of global errors. The density determined from upper hybrid frequency measurements represents another potential source of large errors, which are reported as much as 10%, and even much larger when plasmatrough is considered. Even if more and more sophisticated machine learning tools combined with manual monitoring are constantly developed to accurately evaluate plasma density (e.g., Allison et al., 2021; Zhelavskaya et al., 2021), the complexity persists, particularly during high geomagnetic activity. While the changes provided with the new parametrization seem to be small, they remain nonnegligible since the differences with the previous C&A\* parametrization can attain  $10 \text{ cm}^{-3}$  during magnetic local night times at altitudes of 6 Re. In addition, precise estimations of plasmatrough electron densities are crucial for the different types of waves in the inner magnetosphere that interact with cold plasma population. These interactions have a considerable impact on the dynamics of the high energy particles of the Van Allen radiation belts (Pierrard et al., 2020; Pierrard, Ripoll, et al., 2021). Such interactions justify the search for more accurate modeling of this challenging region. This intertwined system is of principal interest for the current H2020 SafeSpace project (<https://www.safespace-h2020.eu/>), for which an accurate description of the plasmatrough is essential to model the diffusive effects and improve the Van Allen radiation belts characterization.

The results show the need to consider the plasmopause as a boundary layer with a thickness more than a simple sharp limit for long-term density comparisons. By considering a vestigial plasmopause, refilling can be taken into account for recovery periods after storm erosion. This is done using the SPM model for case studies, but

an automatic implementation of the refilling process for all recovery periods would contribute to improve the global simulations and better represent all real situations. Inside such plasmasphere boundary layer, the density evolves as a function of the radial distance from the inner edge to the outer one. Nevertheless, the inclusion of these effects will not have a noticeable influence on the density distribution in the plasmatrough at very large distance, typically at  $L > 6$ , where the plasmatrough is more clearly separated from the plasmasphere, but where no observations are provided neither by Van Allen Probes nor by Arase.

## Data Availability Statement

RBSP/EMFISIS data can be found at: <https://emfisis.physics.uiowa.edu/Flight/>. ARASE data can be found at: <https://ergsc.isee.nagoya-u.ac.jp/data/ergsc/satellite/erg/pwe/>. Science data of the ERG (Arase) satellite were obtained from the ERG Science Center operated by ISAS/JAXA and ISEE/Nagoya University (<https://ergsc.isee.nagoya-u.ac.jp/index.shtml.en>, Miyoshi, Hori, et al., 2018). The present study analyzed PWE-HFA L3 1min v01\_02 data (<https://doi.org/10.34515/DATA.ERG-10001>) and Orbit L2 v03 data (<https://doi.org/10.34515/DATA.ERG-12000>). Kp data can be obtained from <https://ftp.gfz-potsdam.de/pub/home/>.

## References

- Allison, H. J., Shprits, Y. Y., Zhelavskaya, I. S., Wang, D., & Smirnov, A. G. (2021). Gyroresonant wave-particle interactions with chorus waves during extreme depletions of plasma density in the Van Allen radiation belts. *Science Advances*, 7(5), eabc0380. <https://doi.org/10.1126/sciadv.abc0380>
- Bilitza, D. (2018). IRI the international standard for the ionosphere. *Advances in Radio Science*, 16, 1–11. <https://doi.org/10.5194/ars-16-1-2018>
- Bonett, D. G., & Wright, T. A. (2000). Sample size requirements for estimating Pearson, Kendall and Spearman correlations. *Psychometrika*, 65(1), 23–28. <https://doi.org/10.1007/BF02294183>
- Bortnik, J., Li, W., Thorne, R. M., & Angelopoulos, V. (2016). A unified approach to inner magnetospheric state prediction. *Journal of Geophysical Research: Space Physics*, 121, 2423–2430. <https://doi.org/10.1002/2015JA021733>
- Carpenter, D. L., & Anderson, R. R. (1992). An ISEE/whistler model of equatorial electron density in the magnetosphere. *Journal of Geophysical Research*, 97(A2), 1097–1108. <https://doi.org/10.1029/91JA01548>
- Carpenter, D. L., & Lemaire, J. (2004). The plasmasphere boundary layer. *Annales Geophysicae*, 22(12), 4291–4298. <https://doi.org/10.5194/angeo-22-4291-2004>
- Chu, X., Bortnik, J., Li, W., Ma, Q., Denton, R., Yue, C., et al. (2017). A neural network model of three-dimensional dynamic electron density in the inner magnetosphere. *Journal of Geophysical Research: Space Physics*, 122, 9183–9197. <https://doi.org/10.1002/2017JA024464>
- Darrouzet, F., De Keyser, J., Dacrau, P. M. E., El Lemdani-Mazouz, F., & Vallières, X. (2008). Statistical analysis of plasmaspheric plumes with Cluster/WHISPER observations. *Annales Geophysicae*, 26(8), 2403–2417. <https://doi.org/10.5194/angeo-26-2403-2008>
- Darrouzet, F., De Keyser, J., & Pierrard, V. (Eds.). (2009). *The Earth's plasmasphere: A CLUSTER and IMAGE perspective*. Springer Science & Business Media. <https://doi.org/10.1007/978-1-4419-1323-4>
- Darrouzet, F., Gallagher, D. L., André, N., Carpenter, D. L., Dandouras, I., Décréau, P. M. E., et al. (2009). Plasmaspheric density structures and dynamics: Properties observed by the CLUSTER and IMAGE missions. *Space Science Reviews*, 145(1–2), 55–106. <https://doi.org/10.1007/s11214-008-9438-9>
- Darrouzet, F., Pierrard, V., Benck, S., Lointier, G., Cabrera, J., Borremans, K., et al. (2013). Links between the plasmopause and the radiation belt boundaries as observed by the instruments CIS, RAPID, and WHISPER onboard Cluster. *Journal of Geophysical Research: Space Physics*, 118, 4176–4188. <https://doi.org/10.1002/jgra.50239>
- Denton, R. E., Menietti, J. D., Goldstein, J., Young, S. L., & Anderson, R. R. (2004). Electron density in the magnetosphere. *Journal of Geophysical Research*, 109, A09215. <https://doi.org/10.1029/2003JA010245>
- Denton, R. E., Takahashi, K., Galkin, I. A., Nsumei, P. A., Huang, X., Reinisch, B. W., et al. (2006). Distribution of density along magnetospheric field lines. *Journal of Geophysical Research*, 111, A04213. <https://doi.org/10.1029/2005JA011414>
- De Pascuale, S., Jordanova, V. K., Goldstein, J., Kletzing, C. A., Kurth, W. S., Thaller, S. A., & Wygant, J. R. (2018). Simulations of Van Allen Probes plasmaspheric electron density observations. *Journal of Geophysical Research: Space Physics*, 123, 9453–9475. <https://doi.org/10.1029/2018JA025776>
- Gallagher, D. L., Comfort, R. H., Katus, R. M., Sandel, B. R., Fung, S. F., & Adrian, M. L. (2021). The breathing plasmasphere: Erosion and refilling. *Journal of Geophysical Research: Space Physics*, 126, e2020JA028727. <https://doi.org/10.1029/2020JA028727>
- Goldstein, J., Pascuale, S. D., Kletzing, C., Kurth, W., Genestreti, K. J., Skoug, R. M., et al. (2014). Simulation of Van Allen Probes plasmopause encounters. *Journal of Geophysical Research: Space Physics*, 119, 7464–7484. <https://doi.org/10.1002/2014JA020252>
- Guo, D., Fu, S., Xiang, Z., Ni, B., Guo, Y., Feng, M., et al. (2021). Prediction of dynamic plasmopause location using a neural network. *Space Weather*, 19, e2020SW002622. <https://doi.org/10.1029/2020SW002622>
- Hasegawa, T., Matsuda, S., Kumamoto, A., Tsuchiya, F., Kasahara, Y., Miyoshi, Y., et al. (2019). Automatic electron density determination by using a convolutional neural network. *IEEE Access*, 7, 163384–163394. <https://doi.org/10.1109/ACCESS.2019.2951916>
- Hudson, M. K., Baker, D. N., Goldstein, J., Kress, B. T., Paral, J., Toffoletto, F. R., & Wiltberger, M. (2014). Simulated magnetopause losses and Van Allen Probe flux dropouts. *Geophysical Research Letters*, 41, 1113–1118. <https://doi.org/10.1002/2014GL059222>
- Kasahara, Y., Kasaba, Y., Kojima, H., Yagitani, S., Ishisaka, K., Kumamoto, A., et al. (2018). The Plasma Wave Experiment (PWE) on board the Arase (ERG) satellite. *Earth Planets and Space*, 70(1), 86. <https://doi.org/10.1186/s40623-018-0842-4>
- Kasahara, Y., Kumamoto, A., Tsuchiya, F., Kojima, H., Matsuda, S., Matsuoka, A., et al. (2021). *The PWE/HFA instrument Level-3 electron density data of Exploration of energization and Radiation in Geospace (ERG) Arase satellite*. <https://doi.org/10.34515/DATA.ERG-10001>
- Kletzing, C. A., Kurth, W. S., Acuna, M., MacDowall, R. J., Torbert, R. B., Averkamp, T., et al. (2013). The Electric and Magnetic Field Instrument Suite and Integrated Science (EMFISIS) on RBSP. *Space Science Reviews*, 179, 127–181. <https://doi.org/10.1007/s11214-013-9993-6>

## Acknowledgments

The authors acknowledge the SafeSpace project that received funding from the European Union's Horizon 2020 research and innovation program under grant agreement no. 870437. The authors acknowledge the PITHIA-NRF project that received funding from the European Union's Horizon 2020 research and innovation program under grant agreement no. 101007599. The authors thank the VSWMC (Virtual Space Weather Modelling Center) project.

- Kumamoto, A., Tsuchiya, F., Kasahara, Y., Kasaba, Y., Kojima, H., Yagitani, S., et al. (2018). High frequency analyzer (HFA) of plasma wave experiment (PWE) onboard the Arase spacecraft. *Earth, Planets and Space*, *70*(82). <https://doi.org/10.1186/s40623-018-0854-0>
- Kurth, W. S., De Pascuale, S., Faden, J. B., Kletzing, C. A., Hospodarsky, G. B., Thaller, S., & Wygant, J. R. (2015). Electron densities inferred from plasma wave spectra obtained by the Waves instrument on Van Allen Probes. *Journal of Geophysical Research: Space Physics*, *120*, 904–914. <https://doi.org/10.1002/2014JA020857>
- Lapenta, G., Pierrard, V., Keppens, R., Markidis, S., Poedts, S., Šebek, O., et al. (2013). SWIFF: Space Weather Integrated Forecasting Framework. *Journal of Space Weather and Space Climate*, *3*, A05. <https://doi.org/10.1051/swsc/2013027>
- Lemaire, J. F., & Gringauz, K. I. (1998). *The Earth's plasmasphere*. Cambridge University Press. <https://doi.org/10.1007/978-1-4419-1323-4>
- Lemaire, J. F., & Pierrard, V. (2008). Comparison between two theoretical mechanisms for the formation of the plasmapause and relevant observations. *Geomagnetism and Aeronomy*, *48*(5), 553–570. <https://doi.org/10.1134/S0016793208050010>
- Matsuda, S., Hasegawa, T., Kumamoto, A., Tsuchiya, F., Kasahara, Y., Miyoshi, Y., et al. (2020). Detection of UHR frequencies by a convolutional neural network from Arase/PWE data. *Journal of Geophysical Research: Space Physics*, *125*, e2020JA028075. <https://doi.org/10.1029/2020JA028075>
- Matsuoka, A., Teramoto, M., Nomura, R., Nosé, M., Fujimoto, A., Tanaka, Y., et al. (2018). The ARASE (ERG) magnetic field investigation. *Earth, Planets and Space*, *70*(43). <https://doi.org/10.1186/s40623-018-0800-1>
- Matzka, J., Stolle, C., Yamazaki, Y., Bronkalla, O., & Morschhauser, A. (2021). The Geomagnetic *Kp* Index and Derived Indices of Geomagnetic Activity. *Space Weather*, *19*(5). <https://doi.org/10.1029/2020sw002641>
- Mauk, B. H., Fox, N. J., Kanekal, S. G., Kessel, R. L., Sibeck, D. G., & Ukhorskiy, A. (2013). Science objectives and rationale for the radiation belt storm probes mission. *Space Science Reviews*, *179*, 3–27. <https://doi.org/10.1007/s11214-012-9908-y>
- McIlwain, C. E. (1966). *Measurements of trapped electron intensities made by the explorer XV satellite* (pp. 593–609). Springer. [https://doi.org/10.1007/978-94-010-3553-8\\_43](https://doi.org/10.1007/978-94-010-3553-8_43)
- Miyoshi, Y., Hori, T., Shoji, M., Teramoto, M., Chang, T. F., Segawa, T., et al. (2018). The ERG science center. *Earth, Planets and Space*, *70*(96). <https://doi.org/10.1186/s40623-018-0867-8>
- Miyoshi, Y., Shinohara, I., Takashima, T., Asamura, K., Higashio, N., Mitani, T., et al. (2018). Geospace exploration project ERG. *Earth Planets and Space*, *70*(1), 1–13. <https://doi.org/10.1186/s40623-018-0862-0>
- Pierrard, V., Botek, E., & Darrouzet, F. (2021). Improving predictions of the 3D dynamic model of the plasmasphere. *Frontiers in Astronomy and Space Sciences*, *8*(69), 1–8. <https://doi.org/10.3389/fspas.2021.681401>
- Pierrard, V., Botek, E., Ripoll, J. F., & Cunningham, G. (2020). Electron dropout events and flux enhancements associated with geomagnetic storms observed by PROBA-V/energetic particle telescope from 2013 to 2019. *Journal of Geophysical Research: Space Physics*, *125*, e2020JA028487. <https://doi.org/10.1029/2020JA028487>
- Pierrard, V., & Cabrera, J. (2005). Comparisons between EUV/IMAGE observations and numerical simulations of the plasmapause formation. *Annales Geophysicae*, *23*(7), 2635–2646. <https://doi.org/10.5194/angeo-23-2635-2005>
- Pierrard, V., Goldstein, J., André, N., Jordanova, V. K., Kotova, G. A., Lemaire, J. F., et al. (2009). Recent progress in physics-based models of the plasmasphere. *Space Science Reviews*, *145*(1–2), 193–229. <https://doi.org/10.1007/s11214-008-9480-7>
- Pierrard, V., & Lemaire, J. F. (2001). Exospheric model of the plasmasphere. *Journal of Atmospheric and Solar-Terrestrial Physics*, *63*(11), 1261–1265. [https://doi.org/10.1016/S1364-6826\(00\)00227-3](https://doi.org/10.1016/S1364-6826(00)00227-3)
- Pierrard, V., & Lemaire, J. F. (2004). Development of shoulders and plumes in the frame of the interchange instability mechanism for plasmapause formation. *Geophysical Research Letters*, *31*, L05809. <https://doi.org/10.1029/2003GL018919>
- Pierrard, V., Ripoll, J. F., Cunningham, G., Botek, E., Santolik, O., Thaller, S., et al. (2021). Observations and simulations of dropout events and flux decays in October 2013: Comparing MEO equatorial with LEO polar orbit. *Journal of Geophysical Research: Space Physics*, *126*, e2020JA028850. <https://doi.org/10.1029/2020JA028850>
- Pierrard, V., & Stegen, K. (2008). A three-dimensional dynamic kinetic model of the plasmasphere. *Journal of Geophysical Research*, *113*, A10209. <https://doi.org/10.1029/2008JA013060>
- Pierrard, V., & Voiculescu, M. (2011). The 3D model of the plasmasphere coupled to the ionosphere. *Geophysical Research Letters*, *38*, L12104. <https://doi.org/10.1029/2011GL047767>
- Reinisch, B. W., Moldwin, M. B., Denton, R. E., Gallagher, D. L., Matsui, H., Pierrard, V., & Tu, J. (2009). Augmented empirical models of plasmaspheric density and electric field using IMAGE and CLUSTER data. *Space Science Reviews*, *145*, 231–261. <https://doi.org/10.1007/s11214-008-9481-6>
- Sheeley, B. W., Moldwin, M. B., Rassoul, H. K., & Anderson, R. R. (2001). An empirical plasmasphere and trough density model: CRRES observations. *Journal of Geophysical Research*, *106*(A11), 25631–25641. <https://doi.org/10.1029/2000JA000286>
- Verbanac, G., Bandić, M., Pierrard, V., & Cho, J. (2018). MLT plasmapause characteristics: Comparison between THEMIS observations and numerical simulations. *Journal of Geophysical Research: Space Physics*, *123*, 2000–2017. <https://doi.org/10.1002/2017JA024573>
- Zhelavskaya, I. S., Aseev, N. A., & Shprits, Y. Y. (2021). A combined neural network- and physics-based approach for modeling plasmasphere dynamics. *Journal of Geophysical Research: Space Physics*, *126*, e2020JA028077. <https://doi.org/10.1029/2020JA028077>
- Zhelavskaya, I. S., Shprits, Y. Y., & Spasojević, M. (2017). Empirical modeling of the plasmasphere dynamics using neural networks. *Journal of Geophysical Research: Space Physics*, *122*, 227–244. <https://doi.org/10.1002/2017JA024406>